



Functional group scission-induced lattice strain in chiral macromolecular metal-organic framework arrays for electrocatalytic overall water splitting

Yushan Chen^a, Jiakun Wang^a, Zebin Yu^{a,*}, Yanping Hou^a, Ronghua Jiang^b, Mi Wang^a, Jun Huang^c, Jianhua Chen^a, Yongqing Zhang^d, Hongxiang Zhu^e

^a MOE Key Laboratory of New Processing Technology for Nonferrous Metals and Materials, Guangxi Key Laboratory of Processing for Nonferrous Featured Metals and Materials, School of Resources, Environment and Materials, Guangxi University, Nanning 530004, Guangxi, PR China

^b School of Chemical & Environmental Engineering, Shaoguan University, Shaoguan 512005, PR China

^c College of Civil Engineering & Architecture, Guangxi University, Nanning 530004, PR China

^d School of Environment & Energy, Guangdong Provincial Key Laboratory of Atmospheric Environment and Pollution Control, South China University of Technology, Guangzhou 510640, PR China

^e Guangxi Key Laboratory of Clean Pulp & Papermaking and Pollution Control, Nanning 530004, PR China



ARTICLE INFO

Keywords:

Chiral macromolecular metal-organic-framework
Lattice strain
Activation
Functional group
Electrocatalytic overall water splitting

ABSTRACT

Electrocatalytic overall water splitting (OWS) to produce hydrogen and oxygen is one of the most advantageous ways to match the carbon-neutral concept in sustainable hydrogen production. Herein, we report a novel non-precious metal bifunctional electrocatalyst, chiral macromolecular metal-organic frameworks with lattice strain on nickel foam (LS-CMMOFs/NF), by replacing di-sulfonic acid with mono-sulfonic acid for effective and controlled introduction of lattice strain. Under alkaline conditions, LS-CMMOFs/NF at 6% lattice expansion (6% LS-CMMOFs/NF) have the best catalytic performances for oxygen evolution reaction (OER), hydrogen evolution reaction (HER) and OWS, the activity of the catalyst is significantly improved compared with that of the original CMMOFs/NF (O-CMMOFs/NF). The 6%LS-CMMOFs/NF deliver tiny overpotentials of 100 mV (HER), 137 mV (OER), total voltages of 1.467 V (OWS) at 10 mA cm⁻² and maintain100-hours excellent stability. Noteworthy, the OER can reach 500 mA cm⁻², with promising industrial applications. Catalytic mechanism studies, such as operando Raman, operando FTIR and density functional theory calculations indicate that lattice strain effectively enables electrons to pass through Ni/Co 3d-O 2p-Fe 3d more rapidly, thus optimizing metal 3d orbitals, which in turn activates the active surface species (Ni/Co-OOH for OER and Ni/Co-N for HER) and ultimately increases the electrocatalytic activity.

1. Introduction

As society continues to develop, there is an urgent requirement to meet global energy demand while promoting clean and sustainable energy to avoid ongoing ecological degradation [1,2]. Generating environmentally friendly hydrogen energy through electrocatalytic overall water splitting (OWS) has become an essential approach for the straightforward transformation of electrical energy into clean chemical fuels to minimize the emissions of other collateral pollutants [3,4]. Currently, Pt, Ir and Ru-based electrocatalysts are commonly used for their excellent effects in accelerating the reaction kinetics of electrochemical applications. However, the scarcity and poor operational stability seriously hinder their large-scale application [5,6]. Therefore, it is

a long-term goal to explore the earth-abundant, catalytic activity of excellent and stable electrocatalysts.

Metal-organic frameworks (MOFs) have become a promising class of electrocatalysts in latest years owing to their large specific surface area, flexible design and tunable pore channels [7,8]. Nevertheless, the most reported MOFs systems so far still suffer from low mass permeability, low electrical conductivity, low crystallinity and clogging of the active metal centers by organic ligands, which greatly limit their applications as electrocatalysts. Fortunately, the emerging chiral framework materials among different types of MOFs can make the design of various chiral porous materials more convenient and have a strong potential in catalysis because of their expanded pore size range and equally tunable structure and composition [9]. Therefore, a new type of chiral

* Corresponding author.

E-mail addresses: xxzx7514@aliyun.com, xxzx7514@hotmail.com (Z. Yu).

macromolecular metal-organic frameworks (CMMOFs) was prepared by selecting anthraquinone rings with relative molecular masses larger than conventional benzene rings as organic ligands and $\text{-SO}_3\text{Na}$ as the connecting bridges with reference to our previous work, which has been proven to have promising applications in electrochemistry [10]. This is because connecting bridges connect to more metals (connection points called junctions), and the growth of numerous periodic bridges and the increase of junctions will undoubtedly lead to more pores and expanded structures. The expanded structures in CMMOFs also mean more combinations and more excellent tunability, so CMMOFs have more significant porosity, structural diversity and structural tunability compared with conventional small-molecule MOFs. Moreover, the extended structure of CMMOFs also implies higher crystallinity and thus are robust under chemical and physical attack, easily recyclable, dispersed with more good metal active centers and have few topological constraints during crystal and microporous lattice formation [11,12]. Therefore, CMMOFs could be innovative electrocatalysts, undoubtedly providing a new ideal model system to explore the precise structure-performance relationship and design electrochemical catalysts with outstanding catalytic performance and superior stability.

However, by analyzing the internal microstructure and active site of CMMOFs, we found that the dense structure of the catalyst was still easy to inhibit the formation of active sites, and further activation of the catalyst with appropriate strategies may help improve the performance of the catalyst. As we know, lattice strain strategy is very traditional and effective in changing the intrinsic interatomic distance and thus the lattice spacing, affecting the geometry and electronic construction of the active centers, allowing the microstructure to be tuned and ultimately optimizing the electrocatalytic activity of the material [12,13]. For instance, Feng et al. imposed a tensile strain on two-to-three atomic layers of Pt on the intermetallic compound Pt_3Ga to make the combination between OH^* and stretched AL-Pt stronger so that CO^* can be removed more efficiently, and finally improve the oxidation activity [14]. Jiang et al. demonstrated that systematic strain could amplify the synergy between sulfur vacancies and Ru sites to change the catalytic performance of the active site [15]. Nevertheless, the materials in these studies are small molecules, and the strains produced by the materials are randomly formed in the preparation process, so the controllable induced lattice strain and the establishment of internal microscopic strain-activation surface active site relationships in CMMOFs could be a good idea. CMMOFs are formed by connecting functional groups in organic ligands and metal atoms through coordination bonds, it has periodic structural units, so lattice strain might be easily induced by the strategy of breaking functional group linkers in which non-functional group parts replace multiple ordered functional groups. The non-functional groups part of the substituted linker will weaken the interlayer interaction, thus resulting in interlayer expansion.

In this work, we provide a more in-depth study of our previous work, using nickel foam (NF) as a substrate and, for the first time, use a valid but straightforward method of replacing part of the binary sulfonic acid with a monosulfonic acid to induce lattice strain to generate chiral macromolecular metal-organic frameworks under lattice strain based on NF (LS-CMMOFs/NF). Our study aims to evaluate the actual and essential effects of microscopic lattice strain on activated active surface sites at LS-CMMOFs/NF, and establish internal microscopic strain-activated active surface site relationships from the orbital level through DFT theoretical calculations and characterization tests to provide information for tuning and to enhance electrocatalytic activity and stability. As a result, compared with the original CMMOFs/NF (O-CMMOFs/NF) without lattice strain, the lattice strained CMMOFs/NF (LS-CMMOFs/NF, x% is the percentage of lattice expansion) have higher catalytic activity. In 1 M KOH electrolyte, 6%LS-CMMOFs/NF exhibit the lowest overpotential at 10 mA cm^{-2} in HER (100 mV), OER (137 mV) and total voltages in OWS (1.467 V at 10 mA cm^{-2} and 1.85 V at 100 mA cm^{-2}), which are superior to that of O-CMMOFs at 10 mA cm^{-2} in HER (127 mV), OER (182 mV) and OWS (1.546 V). It is worth

mentioning that the lattice strain allows the O-CMMOFs to break through 100 mA cm^{-2} at the same voltage. Moreover, 6%LS-CMMOFs/NF exhibit excellent OER activity over 500 mA cm^{-2} and stability over 100 h, which are very promising for industrial applications. Using advanced operando Raman, operando Fourier transform infrared spectroscopy (operando FTIR) and Density functional theory (DFT) calculations, we observed that the electronic configuration of metal active centers in LS-MMOFs/NF could be adjusted by lattice strain. Lattice strain effectively enables electrons to pass through Ni/Co 3d-O 2p-Fe 3d more rapidly, thus optimizing metal 3d orbitals, which in turn activates the active surface species (Ni/Co-OOH for OER and Ni/Co-N for HER), which increases the electrocatalysis performances.

2. Experiment section

2.1. Chemicals and reagents

Nickel foam (NF), sulfuric acid (H_2SO_4), ethanol ($\text{C}_2\text{H}_6\text{O}$), ferric nitrate ($\text{Fe}(\text{NO}_3)_3 \cdot 9\text{H}_2\text{O}$), cobalt nitrate ($\text{Co}(\text{NO}_3)_2 \cdot 6\text{H}_2\text{O}$), anthraquinone-2,6-disulfonic acid disodium salt ($\text{C}_{14}\text{H}_6\text{Na}_2\text{O}_8\text{S}_2$), sodium anthraquinone-2-sulfonate ($\text{C}_{14}\text{H}_7\text{NaO}_5\text{S}$) and N, N-Dimethyl formamide ($\text{C}_3\text{H}_7\text{NO}$) were purchased from Macklin reagent Co., Ltd.

2.2. Synthesis of catalysts

2.2.1. Synthesis of O-CMMOFs/NF catalysts

Synthesis of O-CMMOFs/NF catalysts: The NF was sonicated in 1 M H_2SO_4 , ethanol and deionized water for 15 min, respectively. In a typical process, The O-CMMOFs/NF were fabricated by dissolving 6 mmol $\text{Co}(\text{NO}_3)_2 \cdot 6\text{H}_2\text{O}$ and 2 mmol $\text{Fe}(\text{NO}_3)_3 \cdot 9\text{H}_2\text{O}$ into 20 ml of deionized water in a reagent bottle, then a slice of NF was immersed into the above solution. After that, 1.0 mmol anthraquinone-2,6-disulfonic acid disodium salt (AQSS) was dispersed in 60 ml $\text{C}_3\text{H}_7\text{NO}$. After minutes of ultrasound, the solution was added to the above solution. Subsequently, the mixed solution was heated 13 h at 120°C , then taken out. The NF was washed with deionized water and ethanol, then dried to get O-CMMOFs/NF.

2.2.2. Synthesis of 4%LS-CMMOFs/NF catalysts

The preparation procedure was the same as that of O-CMMOFs/NF except that a mixture of 0.8 mmol AQSS and 0.2 mmol AQS was used instead of 1.0 mmol AQSS.

2.2.3. Synthesis of 6%LS-CMMOFs/NF catalysts

The preparation procedure was the same as that of O-CMMOFs/NF except that a mixture of 0.6 mmol AQSS and 0.4 mmol AQS was used instead of 1.0 mmol AQSS.

2.2.4. Synthesis of 8%LS-CMMOFs/NF catalysts

The preparation procedure was the same as that of O-CMMOFs/NF except that a mixture of 0.4 mmol AQSS and 0.6 mmol AQS was used instead of 1.0 mmol AQSS.

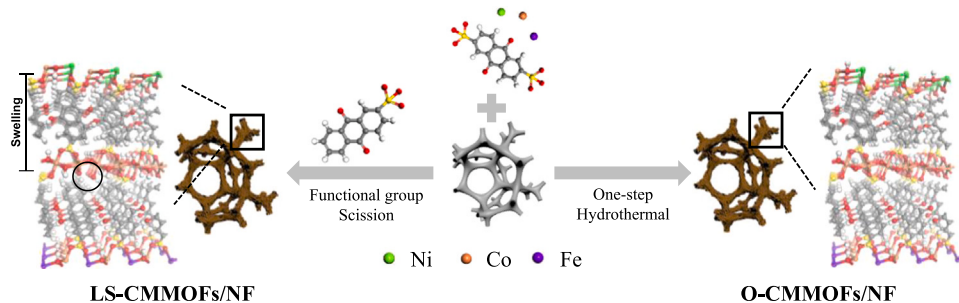
2.2.5. Synthesis of Pt/C/NF and RuO_2/NF catalysts and characterizations and electrochemical measurements

See Supporting information for details.

2.3. Results and discussions

2.3.1. Material characterizations

In this work, monobasic sulfonic acid functional groups replace part of binary sulfonic acid functional groups to break organic linkage molecules, introduce lattice strain into O-CMMOFs/NF and form LS-MMOFs/NF. The O-CMMOFs/NF and LS-CMMOFs/NF nanosheets are grown on NF using a conventional hydrothermal method, and Scheme 1 visualizes the preparation of O-CMMOFs/NF and LS-CMMOFs/NF



Scheme 1. Schematic illustration of the synthesis of O-CMMOFs/NF and LS-CMMOFs/NF.

catalysts. The morphology and structure of these nanosheets can be characterized by field emission scanning electron microscopy (FE-SEM) and high-resolution transmission electron microscopy (HRTEM), as shown in Fig. 1. The HRTEM image in Fig. 1a shows the lattice stripes of the O-CMMOFs/NF nanosheets, so the interlayer spacing between the anthraquinone-based CMMOFs/NF and the transition metal nodes along the [100] direction is determined to be 13.50 Å. In Fig. 1b-d, the interlayer spacings of 4%LS-CMMOFs/NF, 6%LS-CMMOFs/NF and 8% LS-CMMOFs with lattice strain are significantly expanded to 14.04 Å, 14.31 Å and 14.57 Å, corresponding to 4%, 6% and 8% lattice expansions rates, respectively, when binary sulfonic acid functional groups are replaced with different contents of monosulfonic acid functional groups, indicating the successful introduction of lattice strain. The FE-SEM images in Fig. S1 show that, after a simple one-step hydrothermal reaction, the O-CMMOFs/NF form ultrathin nanosheet-like structures with 4–20.5 nm width. Fig. 1e-h show that the LS-CMMOFs/NF morphologies differ little from that of the O-CMMOFs/NF, demonstrating that the lattice-strain strategy does not affect the microscopic morphology while causing changes in the lattice parameters. In addition, as shown in Fig. 1i, elemental mapping images (EDS) of 6%LS-CMMOFs/NF show that all elements are uniformly distributed on the sheet material, which

further provides proof of successful and excellent synthesis. The EDS analysis shows that the Ni/Co/Fe atomic ratio is about 5:3:1 (Table S1), close to the metal content added during the preparation. TEM-EDS of 6% LS-CMMOFs in Fig. S2 also shows the uniform spatial distribution of Fe, Co, Ni, C, O, S and N, further revealing the uniform dispersion of the active sites. Moreover, the atomic ratios of Ni/Co/Fe in O-CMMOFs/NF, 4%LS-CMMOFs/NF, 6%LS-CMMOFs/NF and 8%LS-CMMOFs/NF are also calculated by inductively coupled plasma (ICP) to be all close to 5:3:1 (Table S2).

Fig. 2a and b show the X-ray diffraction (XRD) patterns of the materials, further confirming the successful introduction of lattice strain. It can be seen that all characteristic diffraction peaks of O-CMMOFs/NF and LS-CMMOFs/NF are consistent with theoretical XRD simulations (Simulation), favorably confirming the synthesis of highly crystalline CMMOFs/NF. Moreover, the diffraction angle of the characteristic diffraction peak of O-CMMOFs/NF along the (200) direction is 6.49° , which significantly decreases to 6.33° , 6.15° and 6.03° for the 4%LS-CMMOFs/NF, 6%LS-CMMOFs/NF and 8%LS-CMMOFs/NF with increasing lattice expansion, corresponding to the expansion layer of 14.04 \AA (4%LS-CMMOFs/NF), 14.31 \AA (6%LS-CMMOFs/NF) and 14.57 \AA (8%LS-CMMOFs/NF) along the (200) direction of LS-CMMOFs/

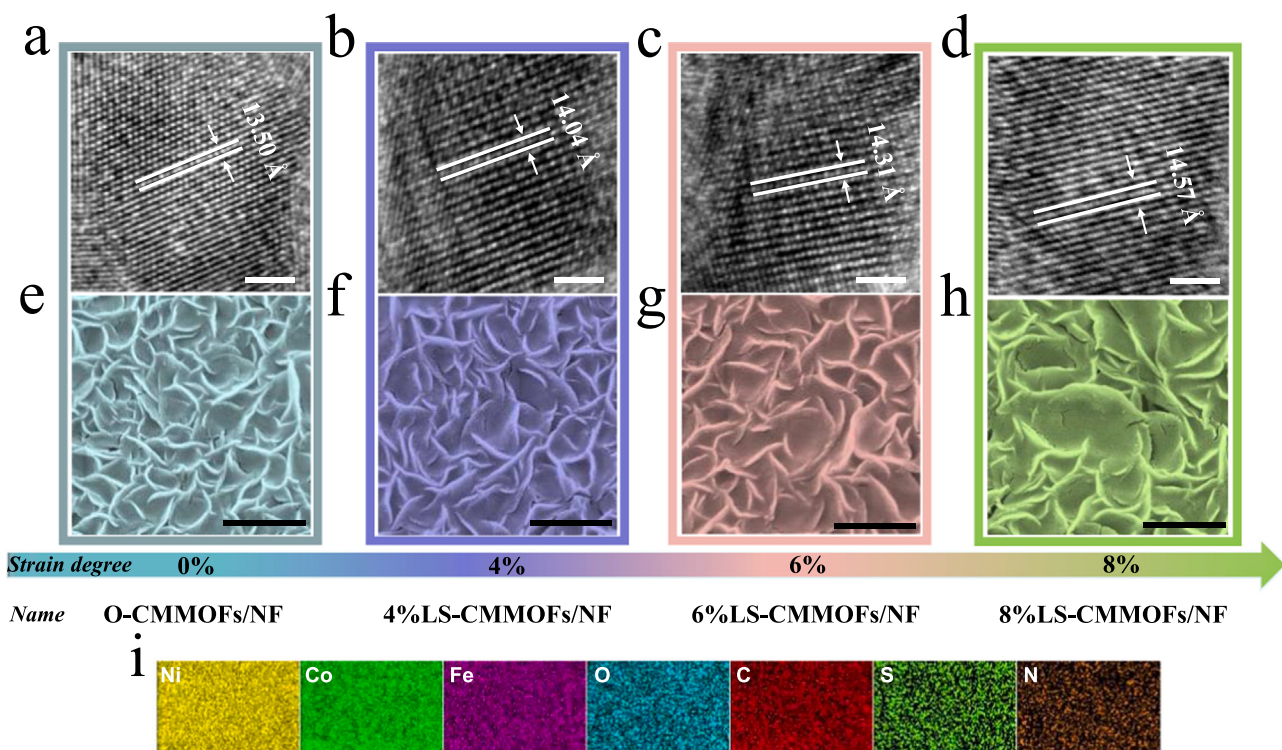


Fig. 1. HRTEM images of the (a) O-CMMOFs/NF, (b) 4%LS-CMMOFs/NF, (c) 6%LS-CMMOFs/NF and (d) 8%LS-CMMOFs/NF. FE-SEM images of the (e) O-CMMOFs/NF, (f) 4%LS-CMMOFs/NF, (g) 6%LS-CMMOFs/NF and (h) 8%LS-CMMOFs/NF. Scale bars, 5 nm for HRTEM and 300 nm for FE-SEM. (i) EDS mapping of Ni, Co, Fe, O, C, S and N obtained from the area in (g).

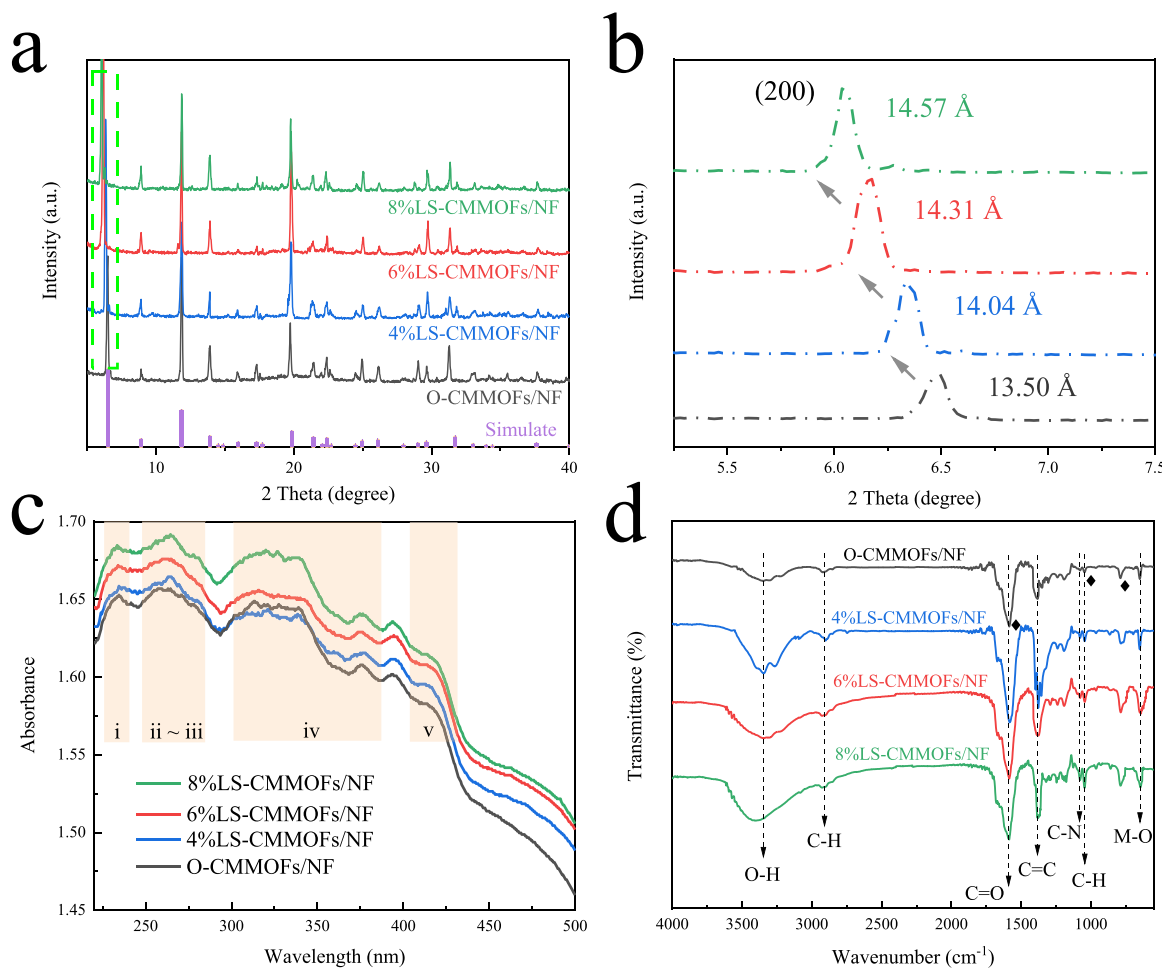


Fig. 2. (a) XRD patterns of O-CMMOFs/NF, 4%LS-CMMOFs/NF, 6%LS-CMMOFs/NF, 8%LS-CMMOFs and Simulate. (b) enlarged XRD patterns. (c) UV-vis and (d) FTIR spectra of O-CMMOFs/NF, 4%LS-CMMOFs/NF, 6%LS-CMMOFs/NF and 8%LS-CMMOFs/NF.

NF. To demonstrate the plausibility of the lattice strain parameter modulation in more depth, we compared the electronic structures of O-CMMOFs/NF and LS-CMMOFs/NF. The optimization results reveal that the absence of functional groups causes the increase of interlayer spacing (Fig. S3), which agrees with the test results of HRTEM and XRD. The lattice parameters indicate that the lattice strain has not affected the crystal phase of the material, corresponding to the smaller offset of XRD (Table S3).

Furthermore, ultraviolet and visible spectrophotometry (UV-vis) is a critical method to determine the structure of Anthraquinone derivatives (AQD), which exhibits peaks in five characteristic absorption ranges representing benzyl and quinonoid structures (230 nm, 240–260 nm, 262–295 nm, 305–389 nm and > 400 nm) [10]. The UV-vis spectrum in Fig. 2c shows that the O-CMMOFs/NF and LS-CMMOFs/NF have peaks in all five characteristic peak-emitting ranges, proving the existence of AQD structures in the CMMOFs/NF materials. Fourier infrared spectroscopy (FTIR) tests were performed to further evidence the synthesis of these materials and to explore their functional groups. (Fig. 2d). The vibration near 3400 cm^{-1} is related to the O-H stretching vibration mode of the absorbed water, and the peaks around 2900 and 1040 cm^{-1} are associated with stretching and bending vibrations of the C—H bond [16,17]. The peak near 1089 cm^{-1} is caused by the stretching and bending vibrations of the C—N bond [10]. The stretching vibrations of M—O result in a peak at about 667 cm^{-1} [16,18]. The presence of absorption peaks at 750, 1044, and 1600 cm^{-1} is good evidence of the existence of the AQD structure, [10,19] further proof that CMMOFs/NF have been successfully synthesized. Combining the experimental results

and theoretical calculations, we can be concluded that we have successfully modulated and synthesized LS-CMMOFs/NF ultrathin nanosheets by a one-step hydrothermal method.

In order to explore the relationship between the surface chemical state and the electrocatalytic performance, the electronic states of the elements in 6%LS-CMMOFs/NF were tested by X-ray photoelectron spectroscopy (XPS). The overall XPS spectrum in Fig. S4 reveals the presence of Ni, Co, Fe, C, S, N and O energy spectrum. Fig. 3a displays the energy spectrum of Ni 2p, showing Ni 2p_{3/2} (855.7 eV), Ni 2p_{1/2} (873.1 eV) and their respective two satellite peaks, respectively, indicating the presence of Ni in the valence state of + 2 [20]. The spectra of Co 2p (Fig. 3b) show Co 2p_{3/2} (781.9 eV) and Co 2p_{1/2} (796.9 eV), attributable to the + 2 valence state of Co, with satellite peaks indicated at 786.9 and 802.0 eV [21]. The spectrum of Fe 2p (Fig. 3c) shows six peaks of Fe 2p_{3/2}: Fe²⁺ (707.8 eV), the satellite peaks of Fe²⁺ (714.2 eV) and Fe³⁺ (722.0 eV), Fe-O (715.1 eV) and Fe³⁺ (711.6 and 718.8 eV) that can be attributed to the partial surface oxidation, which facilitates the acquisition of electrons during the reaction to improve the electron transfer capacity [10,22]. The energy spectrum of C 1s in Fig. 3d includes four prominent characteristic peaks located at 284.0, 284.8, 285.9 and 289 eV, corresponding to C-S, C-C, C-N and C=O, respectively [23]. Fig. 3e displays the energy spectrum of S 2p that the peak at 168.2 eV represents S=O [24]. The energy spectrum of N 1s (Fig. 3f) can be divided into three characteristic peaks: Pyridinic-N (398.8 eV), metal-N (399.6 eV), and Graphitic-N (400.4 eV) [23]. The energy spectrum of O 1s is shown in Fig. 3g, with three distinctive characteristic peaks for lattice oxygen (530.2 eV), oxygen vacancies (531.5 eV) and

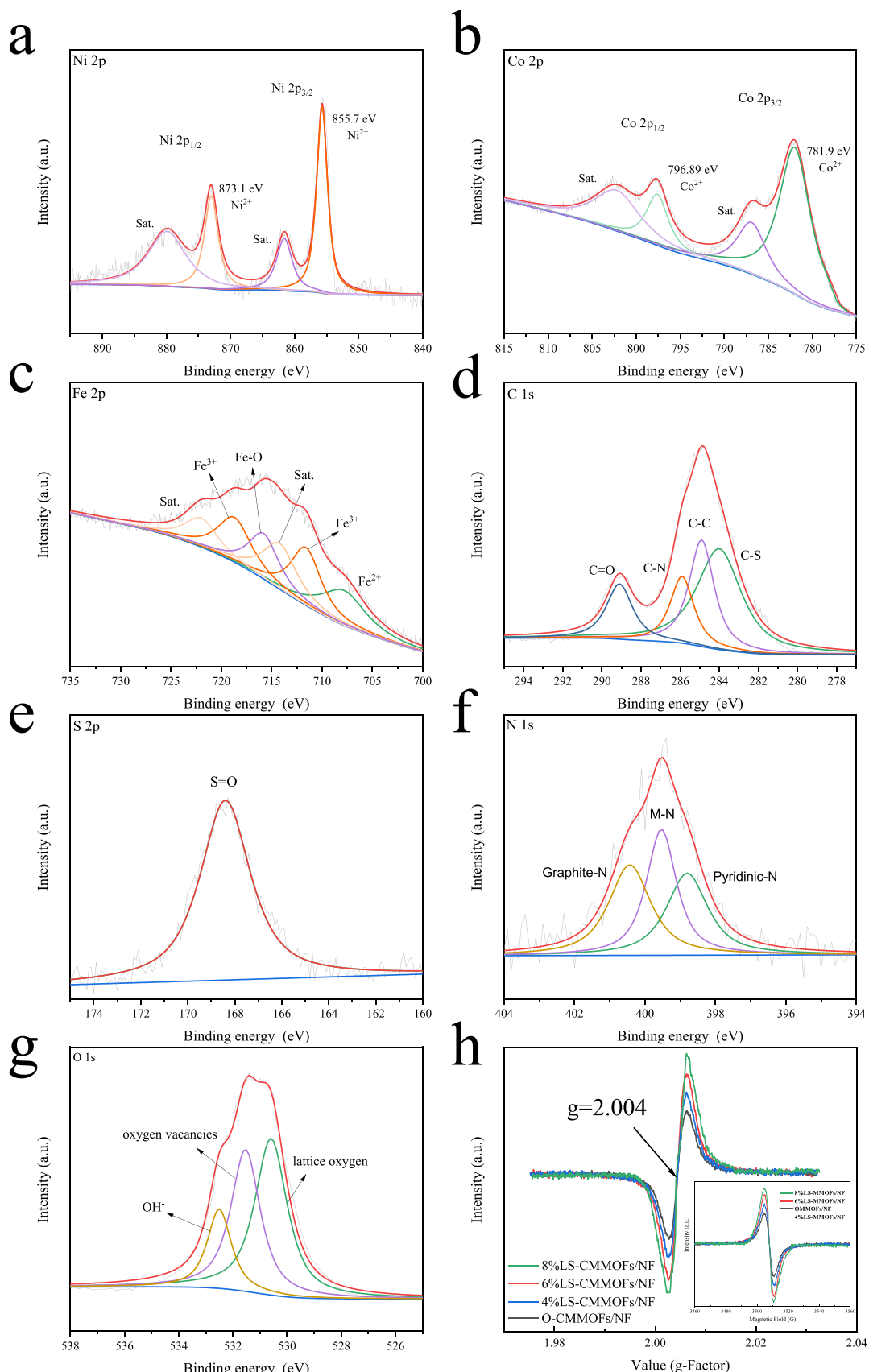


Fig. 3. XPS spectra of the 6%LS-CMMOFs/NF catalyst. (a) Ni 2p, (b) Co 2p, (c) Fe 2p, (d) C 1s, (e) S 2p, (f) N 1s and (g) O 1s (h) EPR spectrum of O-CMMOFs/NF, 4% LS-CMMOFs/NF, 6%LS-CMMOFs/NF and 8%LS-CMMOFs/NF.

adsorbed water species (532.5 eV), [25] indicating that lattice strain achieves the activation of lattice oxygen and generates oxygen defects, both of which are beneficial species for catalytic reactions. Therefore, we infer that the participation of these oxygen species in the OER will generate oxygen species with OER activity, which will promote the catalytic performances of 6%LS-CMMOFs/NF.

We investigated the activate O on the CMMOFs/NF surface by electron paramagnetic resonance (EPR) to confirm O defects further.

Fig. 3h allows us to observe that CMMOFs/NF expose to air have EPR signals with a g-factor of 2.004, indicating the formation of O defects, [25] a finding consistent with the analysis of O 1s in XPS (**Fig. 3g**). By comparison, the enhancement trend of the EPR signal is found to be consistent with the growing trend of the lattice expansion rate of our material, that is, 8%LS-CMMOFs/NF > 6%LS-CMMOFs/NF > 4% LS-CMMOFs/NF > O-CMMOFs/NF, implying that the ability of LS-CMMOFs/NF surface to activate O at room temperature is more

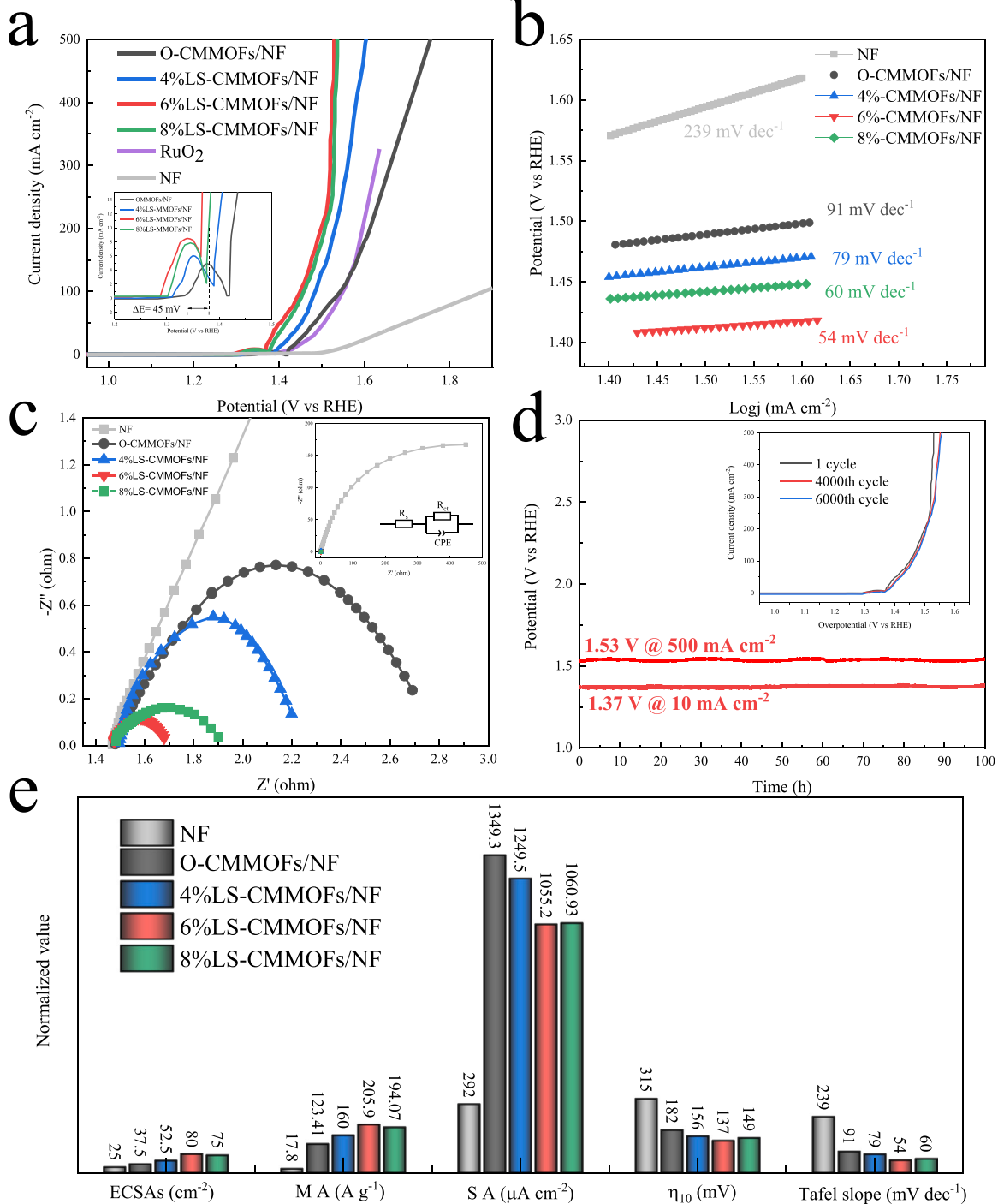


Fig. 4. (a) OER LSV curves (95% iR-corrected) of NF, O-CMMOFs/NF, 4%LS-CMMOFs/NF, 6%LS-CMMOFs/NF, 8%LS-CMMOFs/NF and commercial RuO₂/NF. (b) Tafel plots and (c) EIS tests of NF, O-CMMOFs/NF, 4%LS-CMMOFs/NF, 6%LS-CMMOFs/NF and 8%LS-CMMOFs/NF. (d) The Voltage-time (V-t) curves of 6%LS-CMMOFs/NF for 100 h. Inset: polarization curves for the 6%LS-CMMOFs/NF before and after 4000 and 6000 cycles. (e) The comparisons of ECSAs, mass activity (MA), specific activity (SA), overpotential at 10 mA cm⁻² (η₁₀) and Tafel slope among NF, O-CMMOFs/NF, 4%LS-CMMOFs/NF, 6%LS-CMMOFs/NF and 8%LS-CMMOFs/NF.

potent than that of O-CMMOFs/NF. Notably, previous studies have demonstrated that a moderate amount of defects can provide additional active sites for the material while further activating its surface residual inert substrates, thus increasing the activity of individual sites and favoring a reduction in the overpotential of the reaction [26]. Therefore, we speculate that LS-CMMOFs/NF with lattice strain will have more robust catalytic performances than O-CMMOFs/NF when electrocatalytic water splitting.

2.4. OER performance

OER tests were performed on the four CMMOFs/NF samples using a standard three-electrode system to investigate the effect of lattice strain on the electrocatalytic performances of CMMOFs/NF. We performed electrocatalytic tests by linear scanning voltammetry (LSV) in 1 M KOH electrolyte (95% IR correction). Commercial RuO₂/NF electrocatalysts were tested in same conditions for comparison. The gas produced in the three-electrode system was investigated by gas chromatography. The results confirm that the bubbles produced from the electrode surfaces are only O₂ (Fig. S5). Before testing, we performed LSV tests with different sweep speeds for 6%LS-CMMOFs/NF (Fig. S6) to demonstrate that the sweep speed does not affect the results. As shown in Fig. 4a, the anodic peaks in the OER polarization curves in 1.25–1.45 V (vs. RHE) are ascribed to a higher valence state of Ni, which is derived from the oxidation of Ni²⁺ [27]. In contrast to the O-CMMOFs/NF, the anodic peaks of LS-CMMOFs/NF shifted sequentially to lower potentials by 2–41 mV with increasing lattice strain intensity, and the intensity of the peaks also gradually increased, indicating that LS-CMMOFs/NF have a lower OER activation barrier and more active sites, and 6% LS-CMMOFs/NF showed the best performance. This trend follows the test results of EPR, demonstrating that the activated lattice oxygen caused by the formation of O defects after lattice strain is beneficial for the material, providing additional active sites that facilitate the catalytic reactions of LS-CMMOFs/NF. Consequently, the 6%LS-CMMOFs/NF electrodes require only 137 mV overpotential to achieve a current density of 10 mA cm⁻², outperforming the 8%LS-CMMOFs/NF (149 mV), 4%LS-CMMOFs/NF (156 mV), O-CMMOFs/NF (182 mV) and NF (315 mV) at the same current density. It can be found that the performance of LS-CMMOFs/NF even exceeds that of commercially available RuO₂/NF (202 mV). Besides 10 mA cm⁻², the operating potential at 500 mA cm⁻² is also a key parameter to evaluate the performance of OER, which can show the value of the electrode for commercial applications at high current densities. The 6%LS-CMMOFs/NF electrodes have a very low overpotential of 300 mV at 500 mA cm⁻², much less than 8%LS-CMMOFs/NF (308 mV), 4%LS-CMMOFs/NF (374 mV) and O-CMMOFs/NF (520 mV), while commercially available RuO₂/NF deactivates before it reaches 350 mA cm⁻². We also compared the overpotentials of 6%LS-CMMOFs/NF with most of the electrocatalysts applied in alkaline media at different current densities. Notably, the performance of the materials in this study is significantly better than that of the small-molecule MOFs materials prepared by the lattice strain strategy, showing the great potential of CMMOFs (Table S4).

In addition, we tested the intrinsic properties of 6%LS-CMMOFs/NF by Tafel slope to evaluate the OER catalytic kinetics of CMMOFs/NF. As shown in Fig. 4b, compared to NF (239 mV dec⁻¹), O-CMMOFs/NF (91 mV dec⁻¹), 4%LS-CMMOFs/NF (79 mV dec⁻¹) and 8%LS-CMMOFs/NF (60 mV dec⁻¹) electrodes, 6%LS-CMMOFs/NF electrodes have the 54 mV dec⁻¹ for the lowest Tafel slope, indicating that 6%LS-CMMOFs/NF have superior kinetic performance and faster electron transfer capability during the OER process. Meanwhile, we find that the trend of the Tafel slope of the CMMOFs/NF is slightly different from the trend EPR (Fig. 3h), which is that the kinetic advantage of the material does not increase with the increase of the defect degree (lattice strain rate). The most favorable lattice strain rate to enhance the performance of CMMOFs/NF is about 6%. This result can be attributed to the fact that the proper O defect facilitates the tuning of the electronic structure of

the metal compound and the potential barriers of the intermediates, which effectively enhances the charge transfer and results in the easier absorption of O* intermediates by the metal sites thus causing more O₂ molecules to desorb. The phenomenon belongs to the activation of lattice oxygen during OER, which promotes the formation of highly reactive metal hydroxyl oxides [28,29]. We also performed electrochemical impedance spectroscopy (EIS) tests to inspect the charge transfer process (Fig. 4c). The smallest semicircle radius of the Nyquist curve compared to other materials indicates a lower charge transfer resistance (R_{ct}) for 6%LS-CMMOFs/NF, which could promote faster charge transfer, improved reaction kinetics, and increased capacitive amplification for higher catalytic activity. The specific values of R_{ct} and R_s are shown in Table S5. LSV, Tafel and EIS curves demonstrate that 6% LS-CMMOFs/NF have the best catalytic performance, and the smaller Tafel slope and R_{ct} values of LS-CMMOFs/NF suggest that lattice strain can improve the intrinsic catalytic activity of water by promoting OER kinetics [30]. Electrochemically active specific surface areas (ECSAs) are vital parameters that directly indicate the catalyst's performance for OER, so we performed catalytic oxygen C_{dl} tests to obtain ECSAs from the CV (Fig. S7). As shown in Fig. S8, the C_{dl} of 8%LS-CMMOFs/NF, 6% LS-CMMOFs/NF, 4%LS-CMMOFs/NF, O-CMMOFs/NF and NF were 3.0 mF cm⁻², 3.2 mF cm⁻², 2.1 mF cm⁻², 1.5 mF cm⁻² and 1.0 mF cm⁻², respectively. It is seen that the C_{dl} of the three LS-CMMOFs/NF materials with lattice strain is significantly higher relative to the O-CMMOFs/NF, even more than three times that of the substrate NF, where 6%LS-CMMOFs/NF have the highest effective ECSAs and thus have more effective active sites involved in the reaction, resulting in the best catalytic performance. It is demonstrated that the lattice-strained strategy for preparing unsaturated quinone ring catalysts has apparent advantages and good promotions of O-CMMOFs/NF.

Long-term durability is a severe challenge, especially at high current densities. We measured the durabilities of 6%LS-CMMOFs/NF electrodes operating at current densities of 10 mA cm⁻² and 500 mA cm⁻² for 100 h (h) using chronopotentiometry (V-t). The results show that the performances of the 6%LS-CMMOFs electrodes show no significant degradation after 100 h of operation (Fig. 4d), and the LSV curve shows only a slight change after 6000 cycles (Inset of Fig. 4d), indicating that the 6%LS-CMMOFs/NF have excellent durability in alkaline solutions. The mass activity (M A) also showed the same trend (Fig. 4e). The combined tests show that the 6%LS-CMMOFs/NF materials have excellent electrocatalytic activity and stability when acting on OER.

2.5. HER performance

We also investigated the electrochemical HER activity of several materials in 1 M KOH solutions using a standard three-electrode system, and the datas were corrected for 95% IR. The LSV curves of HER are shown in Fig. 5a, and the 6%LS-CMMOFs/NF possess a minimum overpotential of about 100 mV at a current density of 10 mA cm⁻², which is significantly lower than that of the 8%LS-CMMOFs/NF (107 mV), 4%LS-CMMOFs/NF (113 mV), O-CMMOFs/NF (127 mV), and NF (177 mV). The catalytic kinetics of the materials were tested with Tafel slope, as shown in Fig. 5b, compared with NF (211 mV dec⁻¹), O-CMMOFs/NF (85 mV dec⁻¹), 4%LS-CMMOFs/NF (77 mV dec⁻¹) and 8%LS-CMMOFs/NF (73 mV dec⁻¹), the 6%LS-CMMOFs/NF show a Tafel slope of 72 mV dec⁻¹ with best kinetic advantage. This phenomenon is closely related to the degree of defects caused by lattice strain. The disordered state and activated lattice oxygen caused by a moderate number of O defects tend to cause a decrease in ΔG_H^* , leading to more H* intermediates adsorbed on the active metal sites, thus generating more H₂ molecules [31]. To further understand HER kinetics in charge transfer, we also conducted EIS tests. As shown in the Nyquist curve in Fig. 5c, 6%LS-CMMOFs/NF have the smallest semicircle, representing their smallest R_{ct} , implying that 6% LS-CMMOFs/NF have a significant advantage in charge transfer in terms of reaction kinetics and greater capacitive amplification during HER.

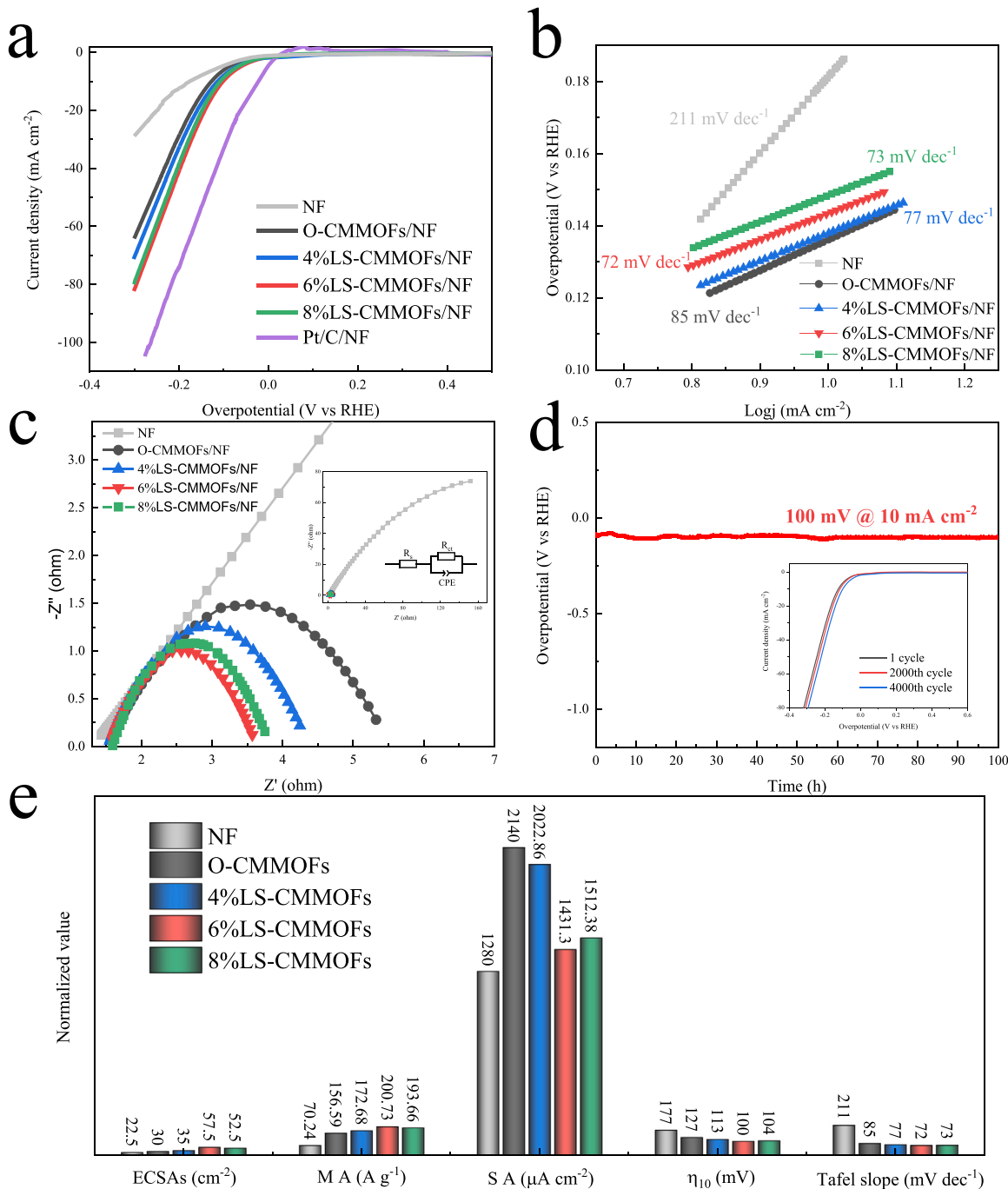


Fig. 5. (a) HER LSV curves (95% iR-corrected) of NF, O-CMMOFs/NF, 4%LS-CMMOFs/NF, 6%LS-CMMOFs/NF, 8%LS-CMMOFs/NF and commercial Pt/C/NF. (b) Tafel plots and (c) EIS tests of NF, O-CMMOFs/NF, 4%LS-CMMOFs/NF, 6%LS-CMMOFs/NF and 8%LS-CMMOFs/NF. (d) The Voltage–time (V–t) curves of 6%LS-CMMOFs/NF for 100 h. Inset: polarization curves for the 6%LS-CMMOFs/NF before and after 2000 and 4000 cycles. (e) The comparisons of ECSAs, mass activity (MA), specific activity (SA), overpotential at 10 mA cm^{-2} (η_{10}) and Tafel slope among NF, O-CMMOFs/NF, 4%LS-CMMOFs/NF, 6%LS-CMMOFs/NF and 8%LS-CMMOFs/NF.

The specific values of R_{ct} and R_{s} are shown in Table S6. Therefore, 6% LS-CMMOFs/NF have the best catalytic performance, corresponding to the LSV curves (Fig. 5a) and Tafel curves (Fig. 5b). It is further demonstrated that the lattice strain has a facilitating effect on the HER kinetic performance of O-CMMOFs/NF.

Finally, the practical application of the 6%LS-CMMOFs/NF catalysts was measured by durability. After measuring the 6%LS-CMMOFs/NF electrode at an applied current of 10 mA cm^{-2} for 100 h using the V-t measurement method, it is found that the electrode did not undergo a significant trend of decay, which once again proves the excellent

durability of 6%LS-CMMOFs/NF in alkaline solutions (Fig. 5d). Then we set up tests with different scan cycles to further study the potential long-term cycling of the 6%LS-CMMOFs/NF (inset of Fig. 5d). After 2000 and 4000 volt-amperes scan cycles, the LSV curves of the 6%LS-CMMOFs/NF change slightly compared to the first cycle, with potential differences of 17 and 26 mV, respectively. In order to explore the inherent catalytic activity of the 6%LS-CMMOFs/NF catalysts for HER, we likewise performed a catalytic oxygen C_{dl} test to obtain ECSAs from CV (Fig. S9). Compared to other substances, the 6%LS-CMMOFs/NF electrodes have the largest C_{dl} of 2.3 mF cm^{-2} (Fig. S10), indicating that 6%LS-

CMMOFs/NF have the largest ECSAs, providing more exposed active sites for HER and thus improving the performance (Fig. 5e). In addition, the trends of M A also matched the lowest overpotential values in the LSV curves (Fig. 5a), further demonstrating the excellent intrinsic catalytic activity of 6%LS-CMMOFs/NF. These results show that 6%LS-CMMOFs/NF can be used as HER catalyst with excellent performance and stability comparable to other non-precious metal-based electrocatalysts reported so far (Table S7).

2.6. OWS performance and characterization

The 6%LS-CMMOFs/NF materials have outstanding OER and HER performance and outstanding durability, so we believe that the 6%LS-CMMOFs/NF materials are expected to be used as ideal bifunctional electrocatalysts for OWS. We tested the 6%LS-CMMOFs/NF||6%LS-CMMOFs/NF electrodes in 1 M KOH using a two-electrode system. The results are displayed in Fig. 6a, 6%LS-CMMOFs/NF||6%LS-CMMOFs/NF cells required only 1.467 V to obtain a current density of 10 mA cm^{-2} , while only 1.85 V is required to reach 100 mA cm^{-2} . It can be seen that the upward trend of the LS-MMOFs/NF is significantly more potent than that of the O-CMMOFs/NF at the later stage, further arguing that the excellent OER and HER performances due to lattice strain-induced O defects also have a strong continuation in the OWS. Potential at other current densities and comparisons with reported superior electrocatalysts are listed in Table S8. In addition, the 6%LS-CMMOFs/NF||6%LS-CMMOFs/NF cells continued the excellent electrochemical durability in the two-electrode system, with no significant degradation in performance at 10 mA cm^{-2} for 100 h (Fig. 6b). Faraday efficiency can measure the percentage of actual generation and theoretical generation to evaluate the energy conversion rate of 6%LS-CMMOFs/NF||6%LS-CMMOFs/NF cells. Therefore, we calculated the molar ratio of H_2 and O_2 during OWS (Fig. 6c). The theoretical data are almost consistent with the experimental data, indicating that the Faraday efficiency is near 100%, proving that the electrocatalytic reaction process 6%LS-CMMOFs/NF||6%LS-CMMOFs/NF have a high energy conversion rate and is precious for application. The above results demonstrate that the innovative electrocatalysts that apply the lattice strain strategy to a novel CMMOFs/NF have excellent catalytic performances and outstanding stabilities, providing a new ideal model system for electrochemical catalysts.

2.7. Mechanism discussion

To further learn the effect of lattice strain on the materials and what changes occur in lattice strained materials during long-term stabilization of HER and OER leading to their excellent electrocatalytic

properties. We carried out a series of characterizations on 6%LS-CMMOFs/NF and O-CMMOFs/NF catalysts through XPS, FE-SEM, XRD, operando Raman, operando FTIR and density functional theory calculations (DFT).

First, we examined the electronic states of the elements in the materials by XPS. As shown in Fig. S11, we first compared the XPS of 6%LS-CMMOFs/NF and O-CMMOFs/NF catalysts. Two significant peaks of Ni 2p are displayed in Fig. S11a, which shifts 0.28 eV to higher energy after lattice strain. Fig. S11b shows the XPS peak of Co 2p, which also shifts to the higher energy after lattice strain by 0.30 eV. On the contrary, the peak of Fe 2p at about 715.7 eV (Fig. S11c) shifts to the lower energy after lattice strain. This result suggests that lattice strain under steady-state conditions will lead to partial electron transfer (from Ni and Co to Fe), which results in more-empty orbitals in Ni, Co and more electrons in orbitals of Fe in LS-CMMOFs/NF. The O 1s XPS peak (Fig. S11d) also shifts to the lower energy after introducing lattice strain, which indicates that some of the electrons are transferred from Ni/Co to Fe via the oxygen of the ligand [1,32]. And the strong interaction between Ni/Co-O-Fe will affect the valence band structure of O-CMMOFs/NF. It can also be found that the peak representing lattice oxygen becomes more significant in the area after the introduction of lattice strain, further demonstrating that lattice strain produces lattice oxygen species that are extremely useful for the catalytic reaction. Fig. S11e-g illustrate that the XPS peaks of C 1s, N 1s and S 2p show energy transfer after introducing lattice strain. These results suggest that lattice strain will affect the electronic states of the elements, which optimizes the valence band structure and ultimately makes the 6%LS-CMMOFs/NF have exceptional performance.

Immediately after, we further analyzed the electronic states of the elements after OER and HER tests to explore what happened to the 6%LS-CMMOFs/NF after the reaction (Fig. S12). After the OER test, the peaks of Ni 2p shifted to higher binding energy by 0.17 eV, and notably, a new peak was detected, corresponding to the characteristic peak of NiOOH (Fig. S12a). The results show that high-priced $\text{Ni}^{3+}/\text{Ni}^{4+}$ is formed on the surface of 6%LS-CMMOFs/NF after OER, which is conducive to realizing an efficient and fast electron transfer process in OER, thus explaining the high OER performance of 6%LS-CMMOFs/NF electrocatalysts [33]. Furthermore, the 6%LS-CMMOFs/NF with three-dimensional nanostructures can offer retarding effects for the continuous generation of NiOOH and contribute to the stability of the materials [10]. After HER testing, the peak of Ni 2p shifts 0.46 eV to higher binding energy, which facilitates the outward transfer of electrons in Ni to non-metallic elements to form a closer bridge connection with them, thus optimizing the metal-nonmetal orbitals and forming an active material favorable to the improved HER performances. As shown in Fig. S12b, the value of Co^{3+} increased significantly after the HER test,

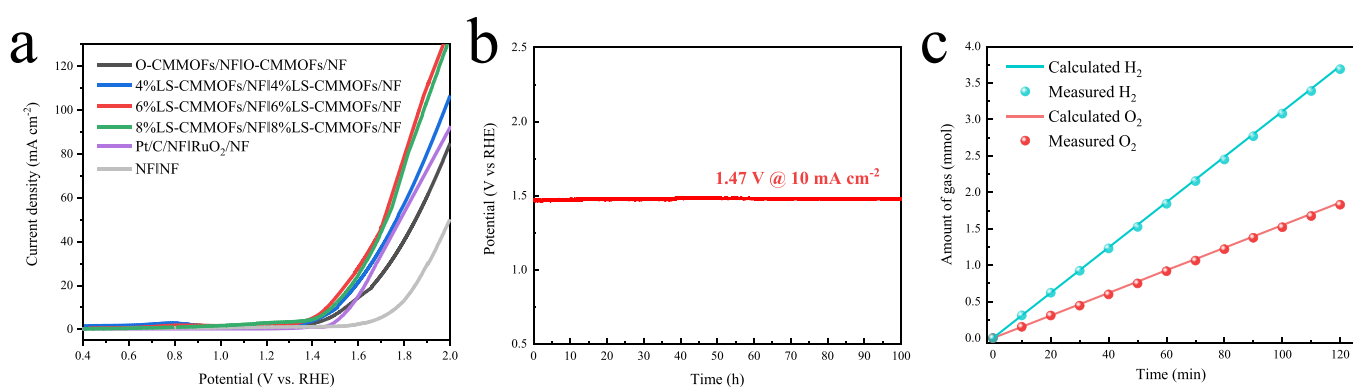


Fig. 6. (a) LSV curves (95% iR-corrected) in the two-electrode configuration. (b) The Voltage–time (V–t) curves of 6%LS-CMMOFs/NF||6%LS-CMMOFs/NF under overall water splitting for 100 h. (c) The amount of H_2 and O_2 produced by the cathode and anode in 1 M KOH solution (the blue and red lines represent the gas evolution at 100% Faradaic efficiency; the blue dots and red dots represent the H_2 and O_2 measured by gas chromatography). (For interpretation of the references to color in this figure legend, the reader is referred to the web version of this article.)

which indicates the existence of electron transfer of Co ions during the cathodic reaction, providing a partial e⁻ source for H⁺→H₂. Meanwhile, the peak of Co-OOH was produced at 784.9 eV after the OER test, [10, 34] and these metal hydroxyl oxides are excellent OER active species. The Fe 2p peaks have no distinct new peak but shift 0.20 eV and 0.25 eV to higher binding energy after HER and OER reactions, respectively (Fig. S12c). The results confirm that the improved OER performances of 6%LS-CMMOFs/NF are strongly correlated with metal hydroxyl oxides. Analysis of the C 1s peak of Fig. S12d revealed the appearance of a new catalytic intermediate π→π* after the reaction, indicating the presence of π-π stacking effect, [10,35] which is because of the local electronic structure change caused by the electron withdrawal from the functional group. Furthermore, the N 1s peak shows a significant decrease in M-N content after the HER test (Fig. S12e), owing to the continuous depletion of M-N as the active site of HER. In the O 1s pattern (Fig. S12f), the peak representing lattice oxygen species shows a trend of weakening peak intensity after both HER and OER, indicating that the lattice oxygen

obtained from the lattice strain strategy of preparing 6% LS-CMMOFs/NF contributes to the catalytic reaction. The S 2p peak (Fig. S12g) shows new peaks at 162.6 and 163.9 eV after HER and OER, which can be identified as S 2p_{3/2} and S 2p_{1/2}, respectively, meaning that the M combines with elemental S during the reaction to produce M-S and S²⁻, [36] which has been shown to have a promising catalytic contribution to catalysis. In summary, the breakage of the functional group as the linker is usually coupled by the loss of the original conjugation effect between the oxygen atom and the anthraquinone ring structure. However, the oxygen atom acts as an intermediary between the various metal atoms to maintain the charge balance, strengthening the metal-metal interaction. Because the primary interaction between Ni/Co and O bridging is e⁻-e⁻ repulsion, and after coupling with Fe, this e⁻-e⁻ repulsion will enhance the original π-donation between Fe-O, which allows the charge transfer from Ni/Co to Fe through O, which is an agreement with the XPS results (Fig. S11). The interaction of the strengthened M-O-M' usually affects the valence band structure of the

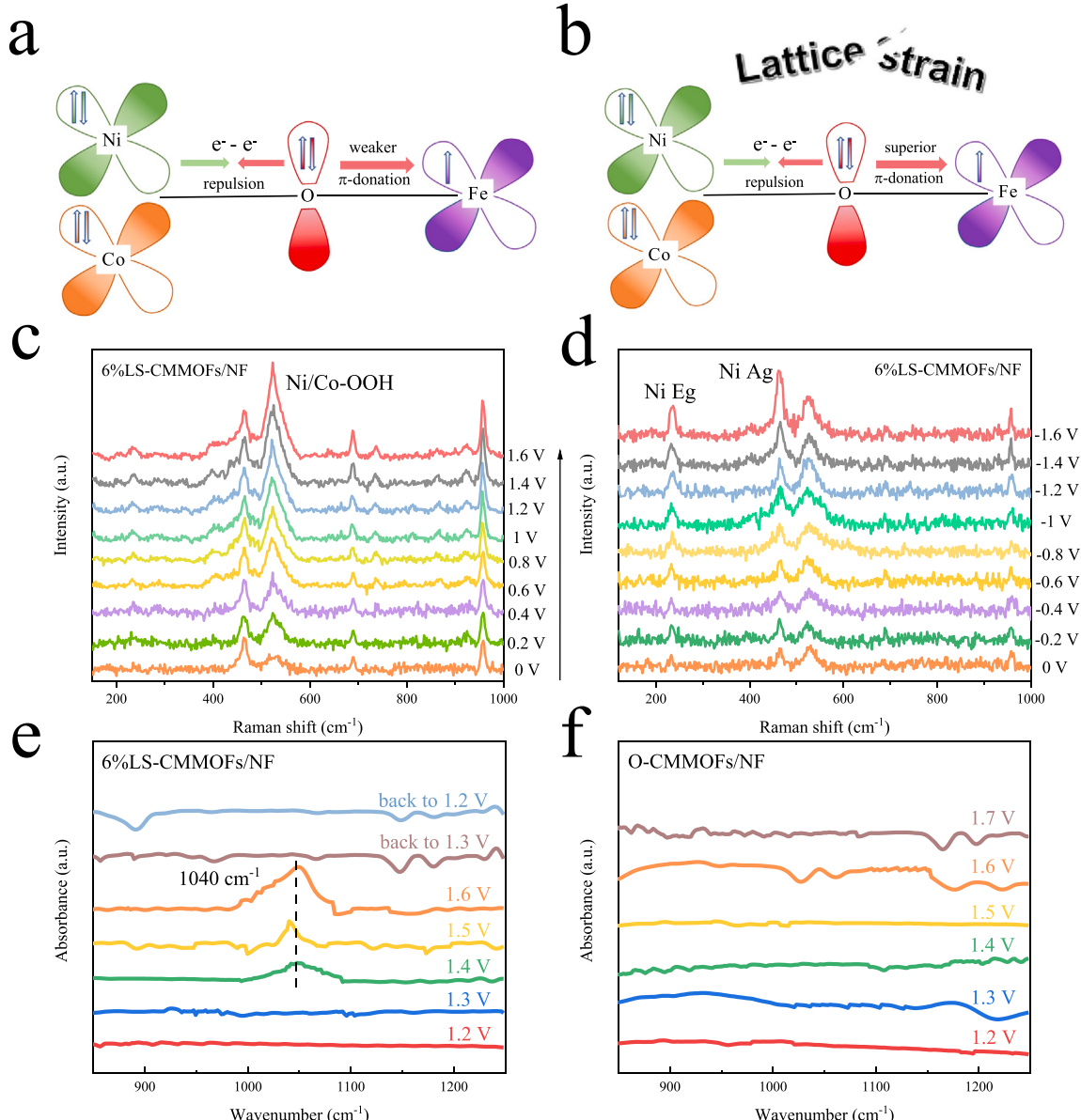


Fig. 7. Schematic representation of the electronic coupling among Ni, Co and Fe in (a) O-CMMOFs/NF and (b) LS-CMMOFs/NF. (c) operando Raman spectra of the 6%LS-CMMOFs/NF collected in the different potential range 0–1.6 V (OER). (d) operando Raman spectra of the 6%LS-CMMOFs/NF collected in the different potential range –1.6–0 V (HER). (e) Operando FTIR spectroscopy measurements for 6%LS-CMMOFs/NF under cycling potential from 1.2 to 1.6 V and back to 1.2 V during the OER process. (f) Operando FTIR spectroscopy measurements for O-CMMOFs/NF under potential from 1.2 to 1.7 V during OER process.

O-CMMOFs/NF (Fig. 7a), while the repulsive force existing between M^{2+} and O^{2-} can have a facilitating effect on the electron transfer, so that a significant change in the electronic state of the metal that can be observed in the XPS energy spectrum. Therefore, it is reasonable to assume that lattice strain can cause electron transfer from Ni^{2+}/Co^{2+} to Fe^{3+} via bridged O^{2-} in 6%LS-CMMOFs/NF (Fig. 7b), thereby transforming the Ni and Co atoms to higher valence states [32]. Ultimately, the optimized electronic structures of metal atoms can effectively generate metal hydroxyl oxides and metal nitrides to boost the performances of 6%LS-CMMOFs/NF in OER and HER.

In the meanwhile, the XRD diffraction peaks after the durability test (Fig. S13) does not detect additional peak signals, indicating that the transition state M-OOH exists in an amorphous state, and the XRD diffraction peaks with little change after the durability test also proves that the 6%LS-CMMOFs/NF have superb stability. We also observed the morphology of 6%LS-CMMOFs/NF after the durability test, as shown in Fig. S14. Compared with the original state (Fig. 1g), 6%LS-CMMOFs/NF nanosheets showed some wear after 100 h of OER (Fig. S14a), and this change is due to the conversion of the contact surface between the material and the electrolyte into M-OOH during the reaction. However, after 100 h of HER, the 6%LS-CMMOFs/NF nanosheets almost maintained their original morphology (Fig. S14b). As seen in the HRTEM image in Fig. S15a, the lattices of 6%LS-CMMOFs/NF after OER stability testing show only a slight distortion, which is related to the strong response of the active site on the OER surface, favoring the excellent OER catalytic activity obtained. In addition, the HRTEM image after HER stability testing in Fig. S15b does not show any significant changes. The results of XRD, FE-SEM and HRTEM proved that 6%LS-CMMOFs/NF are incredibly stable in terms of crystal, surface and lattice structures and are an auspicious material for applications.

To further demonstrate whether the improved OER performances of 6%LS-CMMOFs/NF are correlated with M-OOH, it is crucial to trace the dynamic evolution under actual reaction conditions, so we performed the operando Raman characterization, a characterization method used to test the actual active points of the catalysts in HER and OER. The Raman spectra of 6%LS-CMMOFs/NF immersed in 1 M KOH at selected applied potentials are shown in Fig. 7. In Fig. 7c, clear signals can be observed for 6%LS-CMMOFs/NF in the vibrational frequency region of 150–1000 cm⁻¹. The intensity of the Raman peak located at 525 cm⁻¹ gradually increases as the OER working potential increases from 0 V to 1.6 V. The peak at this location can be attributed to the characteristic peak of M-OOH, [37,38] which indicates that the active site of 6%LS-CMMOFs/NF during OER is the M-OOH. The formation of M-OOH active sites is attributed to the combination of metal cations with OH⁻ anions under alkaline conditions to form M(OH)₂, which is then further converted to M-OOH [39]. Moreover, according to the electron energy shift in XPS (Fig. S12), we obtain that the valence states of Ni and Co are shifted higher, so M-OOH is specifically Ni/Co-OOH. Furthermore, as shown in Fig. 7d, the 6%LS-CMMOFs/NF also undergo a remarkable phase transition during HER. With the change of working potential, the peak intensity at 236.6 cm⁻¹ and 465.5 cm⁻¹ is markedly intensified, and these two peaks are designated as the E_g and A_g phonon models of the Ni Raman feature, respectively [40]. This result proves strong interactions between Ni and Co atoms, [41] while the change of N elements demonstrated in XPS is also closely related. Consequently, operando Raman and XPS evidenced that Ni/Co-OOH and Ni/Co-N are the active centers of OER and HER, respectively. It is obtained by comparison that the operando Raman of O-CMMOFs/NF (Fig. S16) shows a weaker change during OER and HER, which is related to the weaker electron transfer of O-CMMOFs/NF, consistent with the results argued in XPS (Fig. S11). This result is because the Ni/Co-O-Fe are linked in a relatively weak way to obtain the electronic structure, thus inhibiting the Ni/ Co-OOH and Ni/Co-N effective generation. In contrast, the absence of functional groups due to lattice strain in 6%LS-CMMOFs/NF makes the original conjugation effect between anthraquinone ring structures disappear. In order to maintain the charge

balance, the oxygen atoms act as an intermediary between various metal atoms, thus enhancing the metal-metal interactions and Ni/Co-O-Fe interactions and promoting electron transfer resulting in the optimization of the electronic structure. This phenomenon contributes to thermodynamically more favorable binding of surface oxygen species to adjacent metal atoms, thus making it easier to generate Ni/Co-OOH and Ni/Co-N, which are essential for catalysis, and ultimately increasing the catalytic activity.

Since the OER performances of 6%LS-CMMOFs/NF have made a significant contribution to OWS, further justifying the M-OOH active site demonstrated in operando Raman is of great significance, we proceed to perform operando FTIR measurements. As shown in Fig. 7e, no prominent absorption peak is observed in the vibrational frequency region of 850–1250 cm⁻¹ for 6%LS-CMMOFs/NF at a potential of 1.2 V (vs. RHE). However, when the voltage increases to 1.4 V, an absorption peak appears at 1040 cm⁻¹ and becomes more prominent as the voltage increases to 1.6 V. Thus, suggesting that 6%LS-CMMOFs/NF appear as a critical intermediate in the OER process that can be assigned to hydroxyl oxide species of surface intermediate (*OOH) [12,13]. Interestingly, no significant absorption peaks were found in O-CMMOFs/NF at potentials from 1.2 V to 1.6 V or even above 1.6 V in the vibrational frequency region of 850–1250 cm⁻¹ (Fig. 7f). Thus, the presence of unfavorable O-O coupling in O-CMMOFs/NF allows them to undergo a 2e⁻ oxygen-catalyzed process during OER, [42,43] making it more challenging to produce *OOH. In contrast, the active metal sites in LS-CMMOFs/NF can coordinate with the adsorbed water molecules (H₂O^{*}) to rapidly-produce catalytically critical *OOH, [44] which thermodynamically benefits the dissociation/formation of O-O bonds. Thus, LS-CMMOFs/NF undergo an efficient 4e⁻ oxygen catalytic process during OER.

To investigate the OER catalytic mechanism of CMMOFs/NF materials in more depth, we conducted a DFT-based theoretical study. We optimized the structure and measured its interlayer spacing, and the results demonstrated that the absence of functional groups acting as linkers led to an increase in the interlayer spacing (Fig. S3), which is in line with the results of HRTEM (Fig. 1a-d) and XRD (Fig. 2b), and also proved that the structure is highly plausible. The optimized energy band structure calculations in Fig. 8a-b show that LS-CMMOFs/NF have enhanced DOS near the Fermi level, which indicates that LS-CMMOFs/NF have better conductivity than O-CMMOFs/NFs [45,46]. In addition, the density of states results in Fig. S17a-b show that the d-band center energy level of the metal in O-CMMOFs/NF is -1.19 eV, while the d-band center of the metal in LS-CMMOFs/NF moves to a higher energy level (-0.94 eV). According to the d-band theory analysis, it is obtained that the lattice strain enhances the adsorption ability of LS-CMMOFs/NF materials to intermediates [47]. The 3d orbitals of Ni, Co, Fe and 2p orbitals of O atoms in LS-CMMOFs/NF are shown in Fig. S17c-f. It is obtained that the lattice strain makes the M 3d and O 2p orbitals shift towards the vicinity of the Fermi energy level. The analysis of this conclusion in connection with XPS (Fig. S11-S12) shows that the electron transfer of LS-CMMOFs/NF occurs mainly in the M 3d and O 2p orbitals, the lattice strain promotes the electron transfer on the orbitals. The optimized Ni/Co-O-Fe orbitals argued in XPS should be specifically Ni/Co 3d-O 2p-Fe 3d orbitals, where the 3d of metal and 2p of oxygen orbitals move toward the Fermi energy level can promote stronger metal-adsorbate interactions to generate metal hydroxyl oxides and nitrides favorable for catalysis, which ultimately improves the catalytic performance [48]. This result is similar to the reported macromolecular carbon skeleton, so we speculate that the schematic diagram of electron exchange in the energy band structure of LS-CMMOFs/NF is similar to this, as shown in Fig. S18. As shown in Fig. S19, the electron density difference diagrams indicate that electrons are clustered around Fe atoms and depleted around Ni and Co atoms, suggesting electron transfer from Ni/Co to neighboring Fe, which corroborates with the results of XPS (Fig. S11a-c), which would effectively lead to the more preferential adsorption of H and O. This DFT calculation shows that

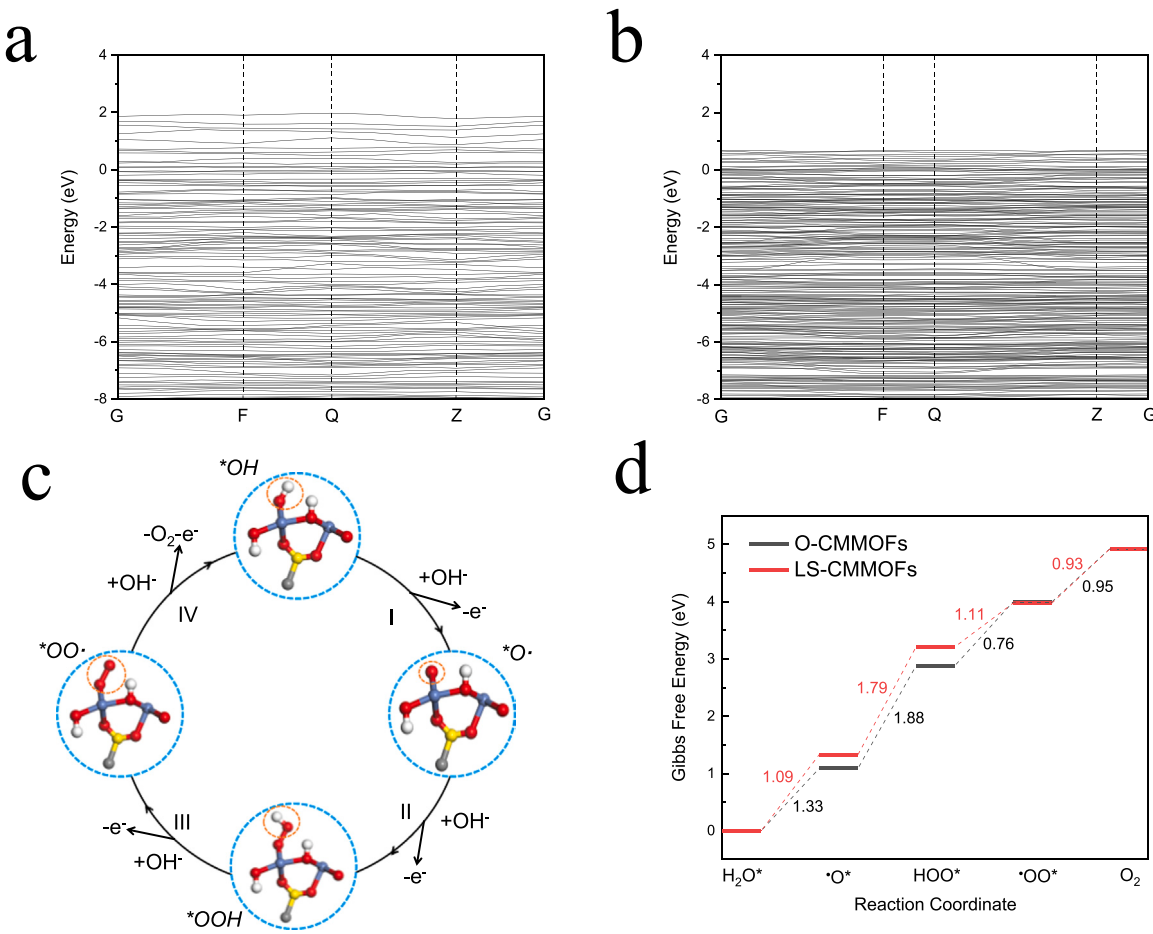


Fig. 8. The calculated energy diagrams for (a) O-CMMOFs/NF and (b) 6%LS-CMMOFs/NF. (c) The schematic theoretical mechanism of the OER cycle processes on the LS-CMMOFs/NF in the alkaline electrolyte. (d) Gibbs free energy change diagram of O-CMMOFs/NF and LS-CMMOFs/NF during the OER process.

CMMOFs/NF enhance the charge intensity around metal atoms by introducing lattice strain, leading to a systematic improvement of OER and HER activity in alkalinity, thus allowing an effective enhancement of H₂O adsorption and optimization of H and O adsorption/desorption. To sum up, O-CMMOFs/NF by introducing lattice should make the breakage of the functional group as a linker, causing the loss of the original conjugation between the oxygen atom and anthraquinone ring structure. Thus, to maintain the charge balance, oxygen atoms will perform as an intermediary between various metal atoms, thus strengthening the metal-metal interaction. Because the primary interaction between Ni/Co and O bridging is e⁻-e⁻ rejection, after lattice strain, this e⁻-e⁻ rejection will enhance the original π-donation between Fe-O, thus allowing charge transfer from Ni/Co to Fe via O, optimizing the Ni/Co-O-Fe orbital, which is argued by PDOS to be specifically a Ni/Co 3d-O 2p-Fe 3d orbitals. The optimized Ni/Co 3d-O 2p-Fe 3d interaction usually affects the valence band structure of O-CMMOFs/NF, while the repulsive force existing between M²⁺ and O²⁻ promotes electron transfer, thus making the Ni 3d and Co 3d orbitals with lower orbital occupancy due to more electron transfer. This phenomenon also leads to Ni 3d and Co 3d orbitals being distributed near the Fermi energy level, facilitating the interaction with surface species to generate hydroxyl oxides and nitrides that are essential for catalysis. This result can lead to a systematic improvement of OER and HER activities under alkaline conditions, which effectively enhances H₂O adsorption and optimization of H and O adsorption/desorption, ultimately yielding a very competitive performance.

Finally, the metal activity towards OER was analyzed by calculating the Gibbs free energy. In the OER process, LS-CMMOFs/NF with lattice

strain effectively reduce the adsorption energy of the active O[·] radicals and thus promote their generation, which would effectively modulate the unfavorable O-O coupling kinetics for a continuous OER. As a result (Fig. 8c and d), the first deprotonation of OH adsorbed on the M site surface occurred, converting the surface M-OH group to M-O[·] (Step I). Next, the M-O[·] group is converted to the superoxide species M-OO[·] (Step II) with ΔG₂ = 1.79 eV, which is much lower than ΔG₂ = 1.88 eV for O-CMMOFs, suggesting that the second adsorption of OH⁻ to form M-OOH is the rate-limiting step of OER, followed by further deprotonation of the superoxide species to produce M-OO[·] (Step III) and finally the release of O₂ molecules to return to the initial state M-OH (Step IV). The molecular catalysts for macromolecular metal organics that have been reported share many similarities with the catalytic mechanism of OER shown in Fig. 8c [49,50]. Therefore, it is further suggested that LS-CMMOFs/NF undergo an efficient and rapid 4e⁻ process similar to that of other macromolecular organics during OER and thus possess excellent performance. Both experimental and theoretical results reveal that the use of lattice strain strategy to modulate the ordered structure of CMMOFs/NF opens a new avenue for developing high-performance electrocatalysts.

3. Conclusions

In summary, we have developed efficient and stable LS-CMMOFs/NF bifunctional electrocatalysts by a controllable and straightforward strategy to induce lattice strain by replacing di-sulfonic acid with mono-sulfonic acid. Mechanistic studies based on electronic structure characterization and theoretical calculations suggest that the electronic

configuration of metal active centers in LS-CMMOFs/NF could be adjusted by lattice strain. The enhanced catalytic performance of LS-CMMOFs/NF is attributed to lattice strain effectively enabling electrons to pass through Ni/Co 3d-O 2p-Fe 3d more rapidly, thus optimizing metal 3d orbitals. This phenomenon activates the active Ni/Co-OOH in the OER process, promoting the reaction and undergoing an efficient and fast 4-electron catalytic process while activating the active Ni/Co-N in the HER process. Therefore 6%LS-CMMOFs/NF exhibit excellent OER, HER and OWS performance in alkaline solutions, requiring only a tiny overpotentials at 10 mA cm⁻² in HER (100 mV), OER (137 mV), total voltages in OWS (1.467 V at 10 mA cm⁻² and 1.85 V at 100 mA cm⁻²), which are superior to that of O-CMMOFs/NF at 10 mA cm⁻² in HER (127 mV), OER (182 mV) and OWS (1.546 V). It is worth mentioning that the lattice strain allows the O-CMMOFs/NF to break through 100 mA cm⁻² at the same voltage. And 6%LS-CMMOFs/NF exhibit excellent OER activity over 500 mA cm⁻² and stability over 100 h, which are very promising for industrial applications. This work evaluates the practical and intrinsic effects of microscopic lattice strain and defects on the activated active surface sites at OWS. It establishes internal microscopic strain-activated active surface site relationships at the orbital level through DFT theoretical calculations and characterization tests to provide information for tuning and to enhance electrocatalytic activity and stability.

CRediT authorship contribution statement

Yushan Chen: Conceptualization, Methodology, Software, Validation, Formal analysis, Investigation, Data curation, Writing – original draft, Writing – review & editing, Visualization. **Jiakun Wang:** Conceptualization, Methodology, Software, Formal analysis, review & editing. **Zebin Yu:** Formal analysis, Conceptualization, Review, Supervision, Project administration, Funding acquisition. **Yanping Hou:** Resources. **Ronghua Jiang:** Resources. **Mi Wang:** Formal analysis, Methodology, Writing – review & editing, Visualization. **Jun Huang:** Resources. **Jianhua Chen:** Resources. **Yongqing Zhang:** Resources. **Hongxiang Zhu:** Resources.

Declaration of Competing Interest

The authors declare that they have no known competing financial interests or personal relationships that could have appeared to influence the work reported in this paper.

Acknowledgments

This research was supported by Open Fund of Guangxi key Laboratory of Processing for Nonferrous Featured Metals and Materials and Open Fund of Guangxi Key Laboratory of Clean Pulp & Papermaking and Pollution Control (No. 2019KF19).

Appendix A. Supporting information

Supplementary data associated with this article can be found in the online version at [doi:10.1016/j.apcatb.2022.121151](https://doi.org/10.1016/j.apcatb.2022.121151).

References

- [1] M. Luo, S. Guo, Strain-controlled electrocatalysis on multimetallic nanomaterials, *Nat. Rev. Mater.* 2 (2017) 17059, <https://doi.org/10.1038/natrevmats.2017.59>.
- [2] L. Yaqoob, T. Noor, N. Iqbal, H. Nasir, N. Zaman, K. Talha, Electrochemical synergies of Fe–Ni bimetallic MOF CNTs catalyst for OER in water splitting, *J. Alloy. Compd.* 850 (2021), 156583, <https://doi.org/10.1016/j.jallcom.2020.156583>.
- [3] Z. Yu, Y. Duan, X. Feng, X. Yu, M. Gao, S. Yu, Clean and affordable hydrogen fuel from alkaline water splitting: past, recent progress, and future prospects, *Adv. Mater.* 33 (2021), 2007100, <https://doi.org/10.1002/adma.202007100>.
- [4] N. Zaman, T. Noor, N. Iqbal, Recent advances in the metal–organic framework-based electrocatalysts for the hydrogen evolution reaction in water splitting: a review, *RSC Adv.* 11 (2021) 21904–21925, <https://doi.org/10.1039/DIKA02240G>.
- [5] S. Anantharaj, Ru-tweaking of non-precious materials: the tale of a strategy that ensures both cost and energy efficiency in electrocatalytic water splitting, *J. Mater. Chem. A* 9 (2021) 6710–6731, <https://doi.org/10.1039/D0TA12424A>.
- [6] F. Gao, Y. Zhang, Z. Wu, H. You, Y. Du, Universal strategies to multi-dimensional noble-metal-based catalysts for electrocatalysis, *Coord. Chem. Rev.* 436 (2021), 213825, <https://doi.org/10.1016/j.ccr.2021.213825>.
- [7] J. Meng, X. Liu, C. Niu, Q. Pang, J. Li, F. Liu, Z. Liu, L. Mai, Advances in metal–organic framework coatings: versatile synthesis and broad applications, *Chem. Soc. Rev.* 49 (2020) 3142–3186, <https://doi.org/10.1039/c9cs00806c>.
- [8] L. Yaqoob, T. Noor, N. Iqbal, H. Nasir, M. Sohal, N. Zaman, M. Usman, Nanocomposites of cobalt benzene tricarboxylic acid MOF with rGO: an efficient and robust electrocatalyst for oxygen evolution reaction (OER), *Renew. Energy* 156 (2020) 1040–1054, <https://doi.org/10.1016/j.renene.2020.04.131>.
- [9] H. Zhang, L.-L. Lou, K. Yu, S. Liu, Advances in chiral metal–organic and covalent organic frameworks for asymmetric catalysis, *Small* 17 (2021), 2005686, <https://doi.org/10.1002/smll.202005686>.
- [10] Y. Chen, Z. Yu, R. Jiang, J. Huang, Y. Hou, J. Chen, Y. Zhang, H. Zhu, B. Wang, M. Wang, 3D-stretched film Ni3S2 nanosheet/macromolecule anthraquinone derivative polymers for electrocatalytic overall water splitting, *Small* 17 (2021), 2101003, <https://doi.org/10.1002/smll.202101003>.
- [11] T. Skorjanc, D. Shetty, A. Trabolsi, Pollutant removal with organic macrocycle-based covalent organic polymers and frameworks, *Chem* 7 (2021) 882–918, <https://doi.org/10.1016/j.chempr.2021.01.002>.
- [12] W. Cheng, X. Zhao, H. Su, F. Tang, W. Che, H. Zhang, Q. Liu, Lattice-strained metal–organic-framework arrays for bifunctional oxygen electrocatalysis, *Nat. Energy* 4 (2019) 115–122, <https://doi.org/10.1038/s41560-018-0308-8>.
- [13] Q. Ji, Y. Kong, C. Wang, H. Tan, H. Duan, W. Hu, G. Li, Y. Lu, N. Li, Y. Wang, J. Tian, Z. Qi, Z. Sun, F. Hu, W. Yan, Lattice strain induced by linker scission in metal–organic framework nanosheets for oxygen evolution reaction, *ACS Catal.* 10 (2020) 5691–5697, <https://doi.org/10.1021/acscatal.0c00989>.
- [14] Q. Feng, S. Zhao, D. He, S. Tian, L. Gu, X. Wen, C. Chen, Q. Peng, D. Wang, Y. Li, Strain engineering to enhance the electrooxidation performance of atomic-layer Pt on intermetallic Pt3Ga, *J. Am. Chem. Soc.* 140 (2018) 2773–2776, <https://doi.org/10.1021/jacs.7b13612>.
- [15] K. Jiang, M. Luo, Z. Liu, M. Peng, D. Chen, Y.-R. Lu, T.-S. Chan, F.M.Fd Groot, Y. Tan, Rational strain engineering of single-atom ruthenium on nanoporous MoS₂ for highly efficient hydrogen evolution, *Nat. Commun.* 12 (2021) 1687, <https://doi.org/10.1038/s41467-021-21956-0>.
- [16] Q. Qian, Y. Li, Y. Liu, L. Yu, G. Zhang, Ambient fast synthesis and active sites deciphering of hierarchical foam-like trimetal-organic framework nanostructures as a platform for highly efficient oxygen evolution electrocatalysis, *Adv. Mater.* 31 (2019), e1901139, <https://doi.org/10.1002/adma.201901139>.
- [17] X. Feng, Y. Song, J.S. Chen, Z. Xu, S.J. Dunn, W. Lin, Rational construction of an artificial binuclear copper monooxygenase in a metal–organic framework, *J. Am. Chem. Soc.* 143 (2021) 1107–1118, <https://doi.org/10.1021/jacs.0c11920>.
- [18] Y. Jiao, Y. Zheng, M. Jaroniec, S.Z. Qiao, Design of electrocatalysts for oxygen- and hydrogen-involving energy conversion reactions, *Chem. Soc. Rev.* 44 (2015) 2060–2086, <https://doi.org/10.1039/c4cs00470a>.
- [19] M. Büschel, C. Stadler, C. Lambert, M. Beck, J. Daub, Heterocyclic quinones as core units for redox switches: UV-vis/NIR, FTIR spectroelectrochemistry and DFT calculations on the vibrational and electronic structure of the radical anions, *J. Electroanal. Chem.* 484 (2000) 24–32, [https://doi.org/10.1016/s0022-0728\(00\)00037-1](https://doi.org/10.1016/s0022-0728(00)00037-1).
- [20] L. Zhang, Y. Zheng, J. Wang, Y. Geng, B. Zhang, J. He, J. Xue, T. Frauenheim, M. Li, Ni/Mo bimetallic-oxide-derived heterointerface-rich sulfide nanosheets with Co-doping for efficient alkaline hydrogen evolution by boosting volmer reaction, *Small* 17 (2021), 2006730, <https://doi.org/10.1002/smll.202006730>.
- [21] M. Feng, J. Huang, Y. Peng, C. Huang, X. Yue, S. Huang, Tuning the electronic structures of cobalt-molybdenum bimetallic carbides to boost the hydrogen oxidation reaction in alkaline medium, *Chem. Eng. J.* 428 (2021), 131206, <https://doi.org/10.1016/j.cej.2021.131206>.
- [22] J. Han, G. Chen, X. Liu, N. Zhang, S. Liang, R. Ma, G. Qiu, Cobalt iron phosphide nanoparticles embedded within a carbon matrix as highly efficient electrocatalysts for the oxygen evolution reaction, *Chem. Commun.* 55 (2019) 9212–9215, <https://doi.org/10.1039/c9cc03117k>.
- [23] Y.S. Kim, G.-H. Lee, B. Ju, D.-W. Kim, TCNQ-derived N/S dual-doped carbon cube electrocatalysts with built-in CoS₂ nanoparticles for high-rate lithium-oxygen batteries, *Chem. Eng. J.* 418 (2021), 129367, <https://doi.org/10.1016/j.cej.2021.129367>.
- [24] S. Chandrasekaran, L. Yao, L. Deng, C. Bowen, Y. Zhang, S. Chen, Z. Lin, F. Peng, P. Zhang, Recent advances in metal sulfides: from controlled fabrication to electrocatalytic, photocatalytic and photoelectrochemical water splitting and beyond, *Chem. Soc. Rev.* 48 (2019) 4178–4280, <https://doi.org/10.1039/c8cs00664d>.
- [25] Z. Li, Q. Yan, Q. Jiang, Y. Gao, T. Xue, R. Li, Y. Liu, Q. Wang, Oxygen vacancy mediated Cu_yCo_{3-y}Fe₁₀O_x mixed oxide as highly active and stable toluene oxidation catalyst by multiple phase interfaces formation and metal doping effect, *Appl. Catal. B* 269 (2021), 118827, <https://doi.org/10.1016/j.apcatb.2020.118827>.
- [26] Y. Yin, J. Han, Y. Zhang, X. Zhang, P. Xu, Q. Yuan, L. Samad, X. Wang, Y. Wang, Z. Zhang, P. Zhang, X. Cao, B. Song, S. Jin, Contributions of phase, sulfur vacancies, and edges to the hydrogen evolution reaction catalytic activity of porous molybdenum disulfide nanosheets, *J. Am. Chem. Soc.* 138 (2016) 7965–7972, <https://doi.org/10.1021/jacs.6b03714>.

- [27] M. Li, Z. Zhao, T. Cheng, A. Fortunelli, C.-Y. Chen, R. Yu, Q. Zhang, L. Gu, B. V. Merinov, Z. Lin, E. Zhu, T. Yu, Q. Jia, J. Guo, L. Zhang, W.A. Goddard, Y. Huang, X. Duan, Ultrafine jagged platinum nanowires enable ultrahigh mass activity for the oxygen reduction reaction, *Science* 354 (2016) 1414–1419, <https://doi.org/10.1126/science.aaf9050>.
- [28] A. Zagalskaya, I. Evazzade, V. Alexandrov, Ab Initio thermodynamics and kinetics of the lattice oxygen evolution reaction in iridium oxides, *ACS Energy Lett.* 6 (2021) 1124–1133, <https://doi.org/10.1021/acsenergylett.1c00234>.
- [29] Y. Zhu, H.A. Tahini, Z. Hu, Z.G. Chen, W. Zhou, A.C. Komarek, Q. Lin, H.J. Lin, C. T. Chen, Y. Zhong, M.T. Fernandez-Diaz, S.C. Smith, H. Wang, M. Liu, Z. Shao, Boosting oxygen evolution reaction by creating both metal ion and lattice-oxygen active sites in a complex oxide, *Adv. Mater.* 32 (2020), e1905025, <https://doi.org/10.1002/adma.201905025>.
- [30] H. Zhang, D. Guan, Z. Hu, Y.-C. Huang, X. Wu, J. Dai, C.-L. Dong, X. Xu, H.-J. Lin, C.-T. Chen, W. Zhou, Z. Shao, Exceptional lattice-oxygen participation on artificially controllable electrochemistry-induced crystalline-amorphous phase to boost oxygen-evolving performance, *Appl. Catal. B* 297 (2021), 120484, <https://doi.org/10.1016/j.apcatb.2021.120484>.
- [31] T.I. Singh, G. Rajeshkanna, U.N. Pan, T. Kshetri, H. Lin, N.H. Kim, J.H. Lee, Alkaline water splitting enhancement by MOF-derived Fe-Co-oxide/Co@NC-mNS heterostructure: boosting OER and HER through defect engineering and in situ oxidation, *Small* 17 (2021), 2101312, <https://doi.org/10.1002/smll.202101312>.
- [32] S. Zhao, Y. Wang, J. Dong, C. He, H. Yin, P. An, K. Zhao, X. Zhang, C. Gao, L. Zhang, J. Lv, J. Wang, J. Zhang, A.M. Khattak, N.A. Khan, Z. Wei, J. Zhang, S. Liu, H. Zhao, Z. Tang, Ultrathin metal-organic framework nanosheets for electrocatalytic oxygen evolution, *Nat. Energy* 184 (2016) 16184, <https://doi.org/10.1038/nenergy.2016.184>.
- [33] G. Chen, Y. Zhu, H. Chen, Z. Hu, S. Hung, N. Ma, J. Dai, H. Lin, C. Chen, W. Zhou, Z. Shao, An amorphous nickel-iron-based electrocatalyst with unusual local structures for ultrafast oxygen evolution reaction, *Adv. Mater.* 31 (2019), 1900883, <https://doi.org/10.1002/adma.201900883>.
- [34] X. Zhang, X. Zhang, H. Xu, Z. Wu, H. Wang, Y. Liang, Iron-doped cobalt monophosphide nanosheet/carbon nanotube hybrids as active and stable electrocatalysts for water splitting, *Adv. Funct. Mater.* 27 (2017), 1606635, <https://doi.org/10.1002/adfm.201606635>.
- [35] C. Li, H. Wu, T. Zhang, Y. Liang, B. Zheng, J. Xia, J. Xu, Q. Miao, Functionalized π stacks of hexabenzoperylenes as a platform for chemical and biological sensing, *Chem* 4 (2018) 1416–1426, <https://doi.org/10.1016/j.chempr.2018.03.007>.
- [36] H. Yang, S. Zhou, B. Zhang, S. Chu, H. Guo, Q. Gu, H. Liu, Y. Lei, K. Konstantinov, Y. Wang, S. Chou, H. Liu, S. Dou, Architecting freestanding sulfur cathodes for superior room-temperature Na-S batteries, *Adv. Funct. Mater.* 31 (2021), 2102280, <https://doi.org/10.1002/adfm.202102280>.
- [37] X. Gao, Y. Yu, Q. Liang, Y. Pang, L. Miao, X. Liu, Z. Kou, J. He, S.J. Pennycook, S. Mu, J. Wang, Surface nitridation of nickel-cobalt alloy nanocactoids raises the performance of water oxidation and splitting, *Appl. Catal. B* 270 (2020), 118889, <https://doi.org/10.1016/j.apcatb.2020.118889>.
- [38] X. Bo, Y. Li, X. Chen, C. Zhao, Operando Raman spectroscopy reveals Cr-induced-phase reconstruction of NiFe and CoFe oxyhydroxides for enhanced electrocatalytic water oxidation, *Chem. Mater.* 32 (2020) 4303–4311, <https://doi.org/10.1021/acs.chemmater.0c01067>.
- [39] J. Dong, F. Zhang, Y. Yang, Y. Zhang, H. He, X. Huang, X. Fan, X. Zhang, (003)-Facet-exposed Ni₃S₂ nanoporous thin films on nickel foil for efficient water splitting, *Appl. Catal. B* 243 (2019) 693–702, <https://doi.org/10.1016/j.apcatb.2018.11.003>.
- [40] Z. Ji, J.L. Liu, Y. Deng, S.Z. Zhang, Z.Z. Zhang, P.D. Du, Y. Zhao, X. Lu, Accurate synergy effect of Ni-Sn dual active sites enhances electrocatalytic oxidation of urea for hydrogen evolution in alkaline medium, *J. Mater. Chem. A* 8 (2020) 14680–14689, <https://doi.org/10.1039/D0TA05160H>.
- [41] J. Hao, H. Liu, Y. Ji, S. Bi, Synthesis and electrochemical performance of Sn-doped LiNi_{0.5}Mn_{1.5}O₄ cathode material for high-voltage lithium-ion batteries, *Sci. China Mater.* 60 (2017) 315–323, <https://doi.org/10.1007/s40843-016-5166-0>.
- [42] D. Guo, R. Shibuya, C. Akiba, S. Saji, T. Kondo, J. Nakamura, Active sites of nitrogen-doped carbon materials for oxygen reduction reaction clarified using model catalysts, *Science* 351 (2016) 361–365, <https://doi.org/10.1126/science.aad0832>.
- [43] E.C.M. Tse, C.J. Barile, N.A. Kirchschlager, Y. Li, J.P. Gewargis, S.C. Zimmerman, A. Hosseini, A.A. Gewirth, Proton transfer dynamics control the mechanism of O₂ reduction by a non-precious metal electrocatalyst, *Nat. Mater.* 15 (2016) 754–759, <https://doi.org/10.1038/nmat4636>.
- [44] Y.P. Zhu, C. Guo, Y. Zheng, S. Qiao, Surface and interface engineering of noble-metal-free electrocatalysts for efficient energy conversion processes, *Acc. Chem. Res.* 50 (2017) 915–923, <https://doi.org/10.1021/acs.accounts.6b00635>.
- [45] L. Yang, L. Huang, Y. Yao, L. Jiao, In-situ construction of lattice-matching NiP₂/NiSe₂ heterointerfaces with electron redistribution for boosting overall water splitting, *Appl. Catal. B* 282 (2021), 119584, <https://doi.org/10.1016/j.apcatb.2020.119584>.
- [46] W. Zhang, Q. Hu, L. Wang, J. Gao, H. Zhu, X. Yan, Z. Gu, In-situ generated Ni-MOF/LDH heterostructures with abundant phase interfaces for enhanced oxygen evolution reaction, *Appl. Catal. B* 286 (2021), 119906, <https://doi.org/10.1016/j.apcatb.2021.119906>.
- [47] S. Sun, X. Zhou, B. Cong, W. Hong, G. Chen, Tailoring the d-band centers endows (Ni_xFe_{1-x})₂P nanosheets with efficient oxygen evolution catalysis, *ACS Catal.* 10 (2020) 9086–9097, <https://doi.org/10.1021/acscatal.0c01273>.
- [48] D. Cao, H. Xu, D. Cheng, Branch-leaf-shaped CuNi@NiFeCu nanodendrites as highly efficient electrocatalysts for overall water splitting, *Appl. Catal. B* 298 (2021), 120600, <https://doi.org/10.1016/j.apcatb.2021.120600>.
- [49] W. Zhang, W. Lai, R. Cao, Energy-related small molecule activation reactions: oxygen reduction and hydrogen and oxygen evolution reactions catalyzed by porphyrin- and corrole-based systems, *Chem. Rev.* 117 (2017) 3717–3797, <https://doi.org/10.1021/acs.chemrev.6b00299>.
- [50] S. Hammes-Schiffer, G. Galli, Integration of theory and experiment in the modelling of heterogeneous electrocatalysis, *Nat. Energy* 6 (2021) 700–705, <https://doi.org/10.1038/s41560-021-00827-4>.